Title
Control of quasi-monoenergetic electron beams from laser-plasma accelerators with adjustable shock density profile

Journal
Physics of Plasmas, 25(4)

ISSN
1070-664X

Authors
Tsai, Hai-En
Swanson, Kelly K
Barber, Sam K
et al.

Publication Date
2018-04-01

DOI
10.1063/1.5023694

Peer reviewed

Control of quasi-monoenergetic electron beams from laser-plasma accelerators with adjustable shock density profile

Hai-En Tsai,[1] Kelly K. Swanson,[1,2] Sam K. Barber,[1] Remi Lehe,[1] Hann-Shin Mao,[1] Daniel E. Mittelberger,[1,2] Sven Steinke,[1] Kei Nakamura,[1] Jeroen van Tilborg,[1] Carl Schroeder,[1] Eric Esarey,[1] Cameron G. R. Geddes,[1] and Wim Leemans[1,2]

[1)] *Lawrence Berkeley National Laboratory, Berkeley, California 94720, USA*

[2)] *Department of Physics, University of California, Berkeley, California 94720, USA*

(Dated: 25 May 2018)

The injection physics in a shock-induced density down-ramp injector was characterized, demonstrating precise control of a laser-plasma accelerator (LPA). Using a jet-blade assembly, experiments systematically varied the shock injector profile, including shock angle, shock position, up-ramp width, and acceleration length. Our work demonstrates that beam energy, energy spread, and pointing can be controlled by adjusting these parameters. As a result, an electron beam that was highly tunable from 25 to 300 MeV with 8% energy spread ($\Delta E_{\mathrm{FWHM}}/E$), 1.5 mrad divergence and 0.35 mrad pointing fluctuation was produced. Particle-in-cell simulation characterized how variation in the shock angle and up-ramp width impacted the injection process. This highly controllable LPA represents a suitable, compact electron beam source for LPA applications such as Thomson sources and free-electron lasers.

I. INTRODUCTION

Laser plasma accelerators (LPAs)[1,2] have become standard tabletop experiments for producing relativistic quasi-monoenergetic electron beams[3–5] from hundreds of MeV[6–8] to above a GeV energy level[9–13] within millimeter to centimeter acceleration lengths. An intense laser pulse ($> 10^{18}$ W/cm^2) propagates through a plasma and generates a plasma wave that can sustain a strong gradient of hundreds of GV/m.[2] In the highly nonlinear bubble regime,[14] electrons are self-trapped due to wavebreaking in the posterior of the bubble and accelerated. However, the instability of this injection mechanism causes fluctuation in beam pointing and beam energy. New LPA-based applications, especially Thomson sources of MeV photons with narrow energy spread,[15–24] free-electron lasers (FELs),[25–27] and multi-stage LPA,[28] demand beams controllable in pointing and energy, and reliable in operation. This raises one of the most important issues with LPAs, which has been how to control the injection of the electrons in the desired location and at the appropriate acceleration phase.

Existing methods for providing injection result in either substantial energy spread or setup complexity. In the ionization injection method,[29–32] a high Z gas or a mixture of high Z and low Z gas is used to provide inner shell electrons in the acceleration region within the middle of the bubble right after the laser peak propagates through it. This produces electron beams (e-beams) with stable pointing and high charge, but at the cost of high divergence and broad energy spread resulting from continuous injection over the acceleration length and laser intensity that remains above threshold. Furthermore, the fundamental limit to ionization injection is high emittance.[33,34] In response to these shortcomings, several techniques to confine the trapping length have been investigated. For example, the use of a mild intensity driving laser[35] and staged gas targets[36–39] resulting in, at best, absolute energy spread of 10 MeV.[37] Experiments[20,40] using a colliding pulse scheme[41,42] have demonstrated precise control of trapping location and energy tunability; however, the addition of a second laser increases the complexity of this method and renders its application difficult in many cases. Hence methods to combine stability, simplicity, and high beam quality are important.

A third method, density down-ramp injection,[43–50] triggering localized injection only in the down-ramp region, provides the possiblity of narrow energy spread, energy tunability, and low emittance. Recent shock-induced down-ramp injection LPAs have achieved high-quality e-beams,[49,50] but beam stability with controlability has not been demonstrated. Furthermore, key parameters that determine e-beam performance: shock angle, up-ramp width, peak density, and shock width of the injector (as discussed in section II), have not been fully measured, analyzed, or optimized.

In this study, we present an experimental and computational analysis of principle physics, including laser self-focusing, electron injection, and beam steering in a shock-induced density down-ramp injector.[46,48–50] Additionally, we greatly expand upon the previously reported experiments[51] and simulations by fully characterizing the shock parameters in correlation to LPA performance. We present four major advances from that previous work.[51] First, a complete comparison is made to identify shock parameters in correlation to e-beam spectrum in two different shock configurations. Second, we demonstrate that, with well-controlled parameters in the straight shock configuration, e-beam stability can be maintained, brightness can be enhanced, energy spread can be reduced and the energy tuning range can be expanded. Third, simulations show that asymmetric injection in the tilted shock causes betatron motion and ex-

plain the beam steering and larger pointing fluctuation observed in the experiment. Fourth, simulations show that broader energy spread produced in wider up-ramp is due to a combination of laser pulse self-steepening, resultant earlier injection, and more pronounced beam loading. We probe these physics effects through simulations using measured shock structures, confirmed by the acceleration results. Advancing previous work, we are able to enhance LPA controllablity and tunability by adjusting the shock parameters. Lets discuss over the coming month the path for the next years or so and the projects, and papers to be written, within it. Im attaching the proposal file, which Hai-En already has. Over the next year and a half we will do several experiments, which are outlined in the statement of work on pages 27-31. Note that some of the deliverable dates have changed from the time when this was submitted due to the continuing resolution so please note dates below.

The overall goal is : Photon source performance will be further increased by continued work on scattering laser guiding as well as LPA control, towards 107photons/shot in 10

Applying these findings, we demonstrate the generation of quasi-monoenergetic e-beams (<10% FWHM energy spread) that are tunable (25−300 MeV central energy) with divergence of 1.5 mrad FWHM and 0.35 mrad pointing stability. We were able to tune e-beam energy by varying blade position or the plasma density, n_e, over a range that preserved narrow energy spread and stable pointing.

Section II describes the principle of shock-induced down-ramp injection. Section III describes the experimental setup, including transverse plasma density and e-beam diagnostics. Section IV presents results for each measurement and the correlation of both measurements. Section V presents particle-in-cell (PIC) simulations and discusses the underlying physics, and Section VI presents conclusions.

II. PRINCIPLES OF SHOCK-INDUCED DOWN-RAMP INJECTION

To avoid the self-trapping instability discussed in Sec. I, controlled trapping is required. For varying plasma conditions, the laser intensities required for self-trapping to occur are derived in the range of $a_0 \simeq 2-4$,[52] where $a_0 = 0.85\sqrt{\lambda_0^2(\mu\mathrm{m})I_0(10^{18}\mathrm{W/cm}^2)}$ is the peak normalized vector potential of the laser wavelength λ_0 and peak intensity I_0, and $a_0 > 1$ defines the relativistic regime. Therefore, if intensity is limited to below self-trapping conditions ($a_0 \approx 1.4$ in our case), an intense wake structure will still be excited but no particles will be self-injected. Under these conditions, controlled trapping can be achieved by lowering the trapping threshold energy via modification of the target structure.

The threshold energy an electron requires in order for it to be trapped in a nonlinear plasma wakefield is:[45,53]

$$\gamma_{th} = \gamma_p(1+\gamma_p\Delta\phi) - \sqrt{{\gamma_p}^2-1}\sqrt{(1+\gamma_p\Delta\phi)^2+1},$$

where γ_p is Lorentz factor associated to plasma phase velocity v_p, and $\Delta\phi = \phi_{max} - \phi_{min}$ is wake amplitude. For a given wakefield amplitude in the accelerating phase, the trapping threshold decreases as v_p decreases. Trapping conditions can be met by providing a density profile consisting of three parts [Fig. 1 (e)]: first, a density up-ramp region across which density increases from 10^{18} cm^3 to n_1, within up-ramp length, L. Second, a short down-ramp region with a density drop in the amount of Δn to n_2. Third, a nearly plateau region of density, n_2, and length, L_{acc}, over which the electrons are accelerated.

In the density up-ramp region, the laser pulse self-focuses and increases in intensity while propagating, providing that laser over critical power ($P > P_{crit}$), and pulse duration approximately equivalent to plasma wavelength λ_p. The plasma electrons are expelled by the ponderomotive force of the laser pulse and a plasma wakefield is generated behind the laser pulse as a result. The background plasma electrons gain momentum closer to trapping threshold as the peak accelerating field increases in the posterior of the bubble. For the parameters of these experiments with moderate a_0, in the up-ramp region, λ_p is shrinking as the laser propagates causing v_p to be high (in many cases v_p is larger than the light speed c) which, in turn, suppresses trapping.

In the down-ramp region, with a steep density drop of Δn, the plasma wavelength λ_p increases with propagation. This causes the expansion of the bubble structure and, as a result, the wake phase front falls further behind the laser. Plasma phase velocity, v_p, decreases due the increase in λ_p, which is a much stronger effect, and hence dominates over the slight increase in laser group velocity, v_g. The decrease of v_p lowers the trapping threshold of background plasma electrons and causes wavebreaking and particle injection in the wakefield of the ramp.[43–45]

In the acceleration region, the bubble expansion stops and the injection is terminated due to the slow varying density plateau, resulting in a highly localized injection. The injected bunch is then accelerated over the length of L_{acc}.

The desired density down-ramp profile can be achieved by gas flow and shock engineering. A shock is created when a supersonic flow encounters an obstruction that turns the flow into itself and compresses it.[54] In this case, a blade placed in the gas jet creates a subsonic region upstream of the blade and is re-expanded with a tilt dictated by the blade position. Due to the mismatch between the jet and the ambient pressure, an under-expanded jet forms which is surrounded by an intercepting shock and its resulting higher density.[55] The boundary of higher density is inclined with respect to the main jet axis as shown in Fig. 1(c). The shock angle, θ_s, changes continuously as the blade moves relative to the jet flow. In addition, the oblique shock intercepts

and modulates the jet density profile as described below in section III. Figure 1 (e) is a representative measured plasma density lineout consisting of an up-ramp region with $L = 1100$ μm and $n_1 = 5.1 \times 10^{18}$ cm^3, a short down-ramp region with a density drop of 2.5×10^{18} cm^3, and an acceleration region with $L_{acc} = 900$ μm and $n_2 = 2.6 \times 10^{18}$ cm^3. As the blade moves further into the gas flow, L increases and L_{acc} decreases with the shock location, as experimentally demonstrated in section IV A.

III. EXPERIMENTAL SETUP

Experiments were performed with the BELLA Center's TREX multi-terawatt Ti:sapphire laser system, which delievered pulses of central wavelength $\lambda_0 = 810$ nm, duration $\tau_{\mathrm{FWHM}} = 45$ fs, repetition rate of 1 Hz, and energy up to 2 J on target. Figure 1(a) shows the setup for this experiment. The s-polarized main pulse entered the target chamber with a rounded top-hat transverse profile with 99% of its energy within an area of 7.0 cm in diameter. A dielectric-coated off-axis parabolic mirror ($f = 200$ cm, $f/30$) focused the beam onto the target. Imaging of the vacuum focus yielded a intensity profile with $w_{\mathrm{FWHM}} = 18 \pm 1 \mu$m (which for a Gaussian profile implies 1/e field profile radius $w_0 = w_{\mathrm{FWHM}}/\sqrt{2 \ln 2} = 15 \pm 1 \mu$m), Strehl ratio > 0.7, and peak intensity up to 4×10^{18} W/cm^2 ($a_0 \approx 1.4$). The uncertainty of the radius indicates rms shot-to-shot fluctuations and spatial asymmetry. The target assembly consisted of a supersonic gas jet and a razor blade. The razor blade was positioned 1.0 mm below the nozzle exit plane and motorized to move independently through the gas flow. The jet and blade assembly was mounted on combined stages allowing x, y, z, and a pivot motion, θ, as shown in Fig. 1(a). The pulsed gas jet was produced with a fast solenoid valve (Parker Pulse Valve) operated at a repetition rate of 1 Hz. The pulse width was set as 1 millisecond using the valve driver. A gas jet with Mach number $M = 2$ was produced from a nozzle with an 800 μm opening which connected by a flexible tube to the valve. The gas jet was set to open such that the laser pulse arrived at the time of peak flow.

In order to characterize this shock injector in situ, a pump-probe plasma density measurement was performed. A 30-mJ probe pulse was split from the main pulse, down-collimated to ~ 1.2 cm beam diameter, and propagated transversely through the plasma target created by the pump laser. The probe pulse was adjusted through a delay line to arrive at the target just after the pump pulse exited the plasma, allowing no time for the shock feature to undergo hydro expansion.[54] For the same reason, the distance between blade and pump laser was set at 1.0 mm in order to preserve shock sharpness and prevent damaging the blade. The shock was imaged by a f/20 lens onto a wave front sensor (SID-4 HR by Phasics Co.) with a 3.0 mm field of view and 30 μm image resolution.[56] Figure 1(b) and (c) show a representative shadowgram and a converted phase map, ϕ(y, z), with the blade covering half of the jet. In the phase map, the low phase region (blue) is neutral gas and the high phase feature (red/green) is plasma ionized by a separate pump pulse resulting in a much higher refractive index. However, the shock front, presenting a sudden phase drop and indicated with a white dashed line, can be observed across both the neutral and plasma regions. The shock front is created by the blade inclined at an angle, θ_s, relative to vertical direction. The plasma density map, n_e(r, z), can be obtained from the phase map, ϕ(y, z). The on-axis density lineout, $n_e(r = 0, z)$ presented in Fig. 1(e), shows a shock with up-ramp width, L, a down-ramp transition from density n_1 to n_2, and acceleration length, L_{acc}. The plasma density, n_e, can be linearly adjusted by gas jet backing pressure. Fig. 1(d) shows the gas jet was operated in a regime (0-120 psi) in which measured density (averaged over 250 shots) scaled linearly with gas jet backing pressure and the density rms fluctuation (error bar) was smaller than 3%.

For e-beam diagnostics, a magnetic electron spectrometer placed downstream from the gas jet analyzed electron energy on each shot. It consisted of a current-tunable magnet that deflected electrons onto terbium-activated gadolinium oxysulfide (Gd_2O_2S:Tb) Lanex phosphor screen[57] from which electron-induced fluorescence at 545 nm was imaged onto an array of 12-bit charge-coupled device (CCD) cameras. Energy spread was determined by taking the ratio of the width, E_{FWHM}, of the quasimonoenergetic peak to its central energy, E_{peak}. For e-beam spatial profile and divergence, a phosphor screen imaged to a CCD camera placed up-stream from a magnetic spectrometer can be switched into the beam line. The e-beam energy spectrum, charge, and beam divergence were determined based on previously published calibrations.[58,59]

IV. RESULTS

A. Shock structure and correlated LPA performance

The shock structure as described in section II was captured on the wavefront sensor. Figures 2(a)–(d) show four frames of the transverse phase structure, as the blade is moved from left to right across the jet at coverages of 10%, 30%, 45%, and 60%, respectively. The shock front was observed to have a density down-ramp width of 50 μm in both neutral and ionized hydrogen (indicated by white dashed lines) independent of blade position and n_e. The shock front angle was observed to increase steeply in direct relationship to increasing blade coverage as explained in Sec. II and predicted by fluid simulations.[54] In addition, as shown in the right column of Figs. 2(a)–(d), the shock-induced peak rises and moves from left to right with increasing blade coverage.

The shock structure, as defined by the parameters: (1)θ_s, (2)L and L_{acc}, (3)$n_1$and Δn, is quantitatively com-

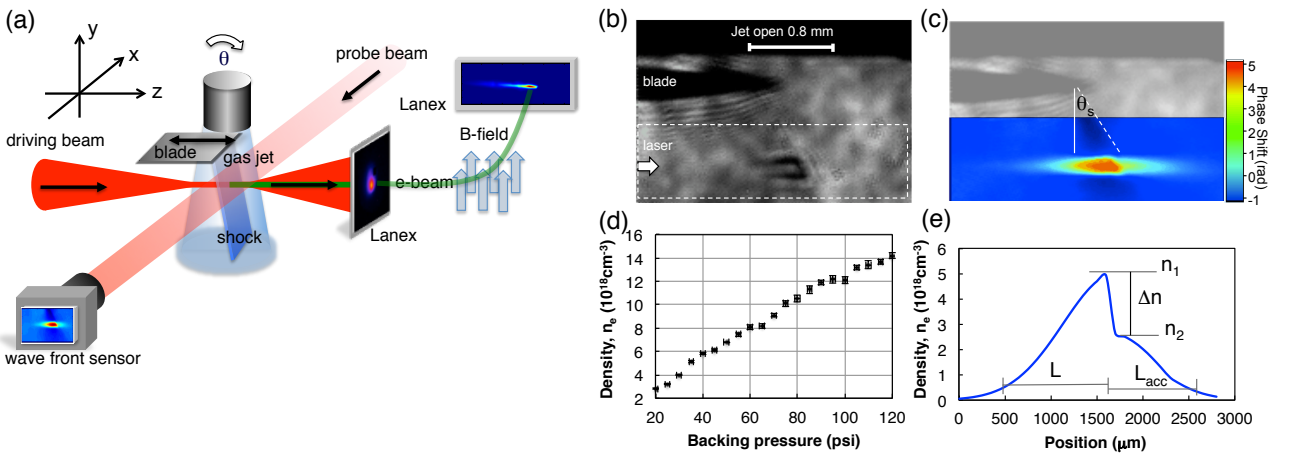

FIG. 1. **(a)** Schematic of experimental setup for shock-injected laser-plasma accelerator (LPA). Interaction of a 2-J drive laser (red) with a plasma created within the plume of a gas jet accelerates electrons (green). A position-controlled razor blade created a density transition (shock) used as an electron injector. The e-beam spatial profiles are recorded by a phosphor screen (Lanex) and e-beam spectra are recorded by a magnetic spectrometer. A 30-mJ transverse beam split from main laser is used to probe the plasma structure, which is then imaged onto a wave front sensor on each shot to obtain, **(b)** the shadowgram, and **(c)** the phase map, ϕ(y, z), retrieved from the dashed area of **(b)**. **(d)** The peak density (averaged over 250 shots) scales linearly with gas jet backing pressure with small rms fluctuation (error bar $< 3\%$).**(e)** The density lineout, $\bar{n}_e(r = 0, z)$, taken along the laser axis of the transformed phase map, shows a shock with up-ramp width, L, a down-ramp transition from density n_1 to n_2, and acceleration length, L_{acc}.

pared to e-beam production in Figs. 2(e)–(g). When the blade moved into the gas jet from 10% to 100%, the shock angle, θ_s, swept linearly from 30 to 60 degrees as shown in Fig. 2(e). The e-beam injection threshold was reached at an oblique angle as the blade covered more than 48% of the jet, as shown in the magnetic spectra inset in Fig. 2(e). This blade position created the steepest shock, where the shock density, n_1, and density drop, Δn, reached their maximum values of 1.1×10^{19} cm^{-3} and 5.0×10^{18} cm^{-3}, respectively. As the blade moved into the jet from 48% to 70%, the n_1 and Δn values stayed nearly constant (90% of their peak) and, therefore, the electrons were injected. In this range, though injector parameters did not change significantly, electron peak energy decreased as the blade coverage increased. This is due to the fact that the location of the shock moves with the blade, increasing L and reducing L_{acc} as shown in Fig. 2(g), an observation linearly correlated to decreasing electron peak energy. However, the e-beam injection threshold was reached in a strongly tilted shock. The resulting e-beam had a 24 pC charge, 45 MeV peak energy, 21% energy spread ($\Delta E_{\rm FWHM}/E$), 3 mrad divergence, and 0.7 mrad pointing stability. The strongly tilted shock not only limited energy tuning range, but also steered the e-beam by $0.6 - 1.5$ mrad.[51] This shock steering effect is explained by the hypothesis that the electrons follow the deflected laser as it propagates through the asymmetric density profiles. This can cause oscillation and degraded e-beam quality, as discussed in Sec. V A.

To achieve a shock orthogonal to the laser axis, a second configuration was introduced in which the jet-blade assembly was pivoted by 30 degrees such that the laser axis was orthogonal to the shock with 50% blade coverage. As shown in Fig. 3(b), this produced an optimum e-beam with 16 pC charge, 80 MeV central energy, 8% energy spread ($\Delta E_{\rm FWHM}/E$), 0.35 mrad pointing stability, and 1.5 mrad divergence. In the straight shock configuration, tuning could be achieved with injection over a broader range of shock angle from -20 degrees to 30 degrees (instead of from 30 degrees to 60 degrees) and e-beam central energy could be tuned from 25 MeV to 125 MeV with $< 10\%$ energy spread, as shown in Fig. 3(d). In the straight shock configuration, the e-beam injection threshold was reached with 40% blade coverage, at a lower peak density (9×10^{18} cm^3) than the maximum peak density. This can be compared to the tilted shock configuration, where injection only occured after 48% coverage. However, a significant charge of > 10 pC and low divergence e-beams were still injected and accelerated at the maximum peak density (1.1×10^{19} cm^3) with 48% blade coverage as seen in the tilted shock configuration. The up-ramp width was significantly reduced from tilted to straight shock configuration. As discussed below, the shock angle strongly correlates to e-beam steering, while up-ramp width correlates to e-beam energy spread.

In the two configurations described above, the shock front was variably angled from 30 to 60 degrees and from -20 to 30 degrees respectively by adjusting the blade position. As we varied the shock angle, electrons were produced and recorded. Pointing was determined by the centroid of the electron spatial profile and we found that the shock angle had a strong correlation with e-beam pointing. Figure 4 presents e-beams steered by shock

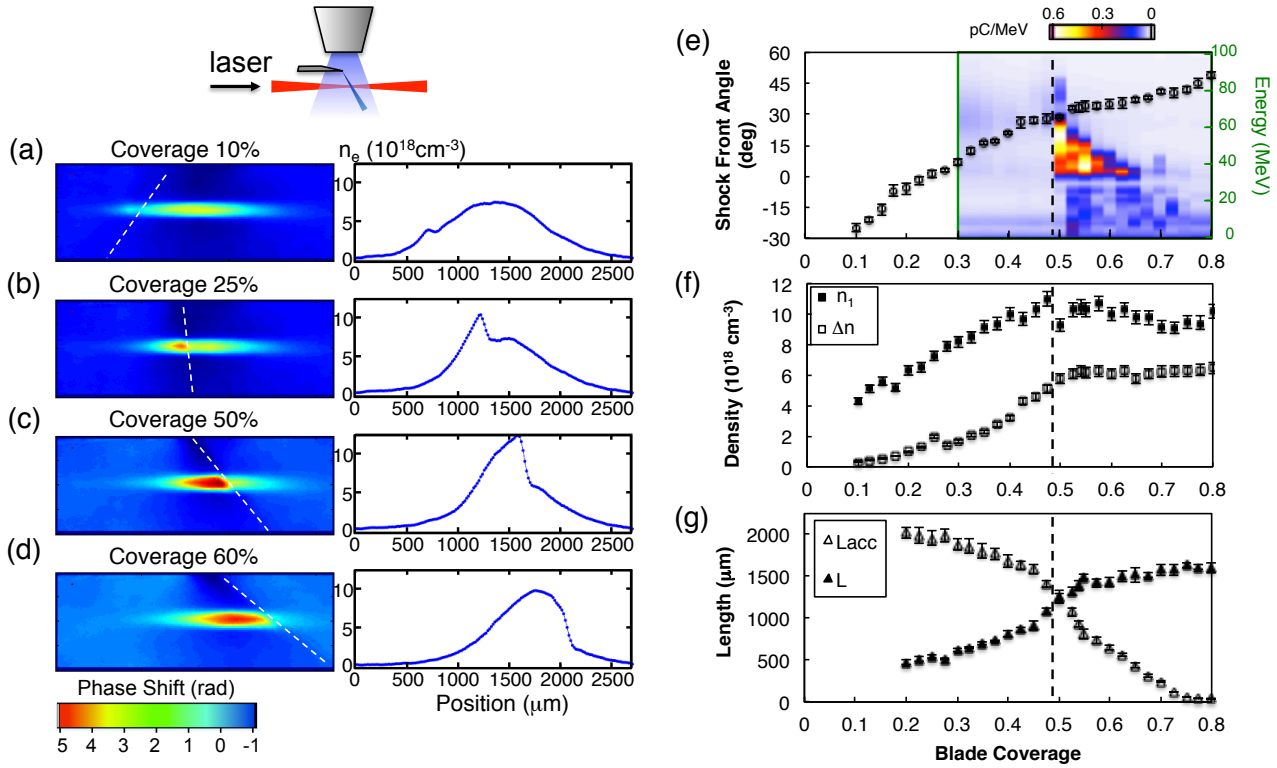

FIG. 2. Phase structure measured by wavefront sensor as the blade was translated through the gas jet. Each row of **(a)**, **(b)**, **(c)**, and **(d)**corresponds to a phase image and horizontal phase lineout at a particular blade coverage. The shock front (indicated with white dashed line) can be seen in both neutral hydrogen and plasma. **(e)** Shock front angle and e-beam magnetic spectra, **(f)** shock density, n_1, and density drop, $\Delta n, (= n_1 - n_2)$ and **(g)** up-ramp with, L, and acceleration length, L_{acc}, versus blade coverage. The electron injection happens when blade coverage is more than 48%, which is indicated with vertical dash line.

angles measured in the two configurations. With the first configuration (white data points), the strongly tilted shock (from 30 to 45 degrees) steered electrons more than 1 mrad from the propagation axis, while the straight shock produced with the second configuration (black data points) steered the electrons back to the center within 1 mrad. While absolute range varies, the dependence on shock angle is consistent. Using measured shock angles and density profiles, the calculated refraction of the laser (dashed line) matched the trend of electron deviation (data points). Three dimensional simulation results (blue squares) using 0 degree and 26 degree shock also agree with these results, as discussed in Sec. V A below. This confirms that shock refraction of the laser is responsible for the observed e-beam steering.

For LPA-based applications or multi-stage experiments, beam stability, repeatibility, and small emittance and divergence are the key requirements. Therefore, the most stable e-beams produced in the two configurations discussed here are compared to each other. The shock front position for the two configurations was different and, therefore, the laser focal position was also adjusted to target the shock region, which was found to be optimal for stable e-beam performance. We found that e-beam performance in the second configuration was significantly better: the shock was nearly straightened and the up-ramp width was reduced at maximum peak density, yielding the smallest divergence and greatest stability. Electron beams were produced with 0.35 mrad rms pointing fluctuation, 2 pC charge fluctuation, 6% energy fluctuation, and 8% energy spread. Figure 5 compares the most stable acceleration results from the first configuration [tilt shock: (a) and (c)] and the second configuration [straight shock: (b) and (d)], demonstrating stability and repeatablity in the straight shock configuration.

B. Tuning of energy and energy spread

With a shock nearly orthogonal to the laser in the straight shock configuration, we found a stable region where energy tunablity can be achieved with significantly reduced energy spread and high repeatibility and stability—performance which cannot be achieved in the tilted shock configuration. Tuning using either blade coverage or plasma density can be achieved to provide a broader energy range. As shown in Fig. 6 (a), by moving the blade position from 55% to 35% coverage (blade scan)

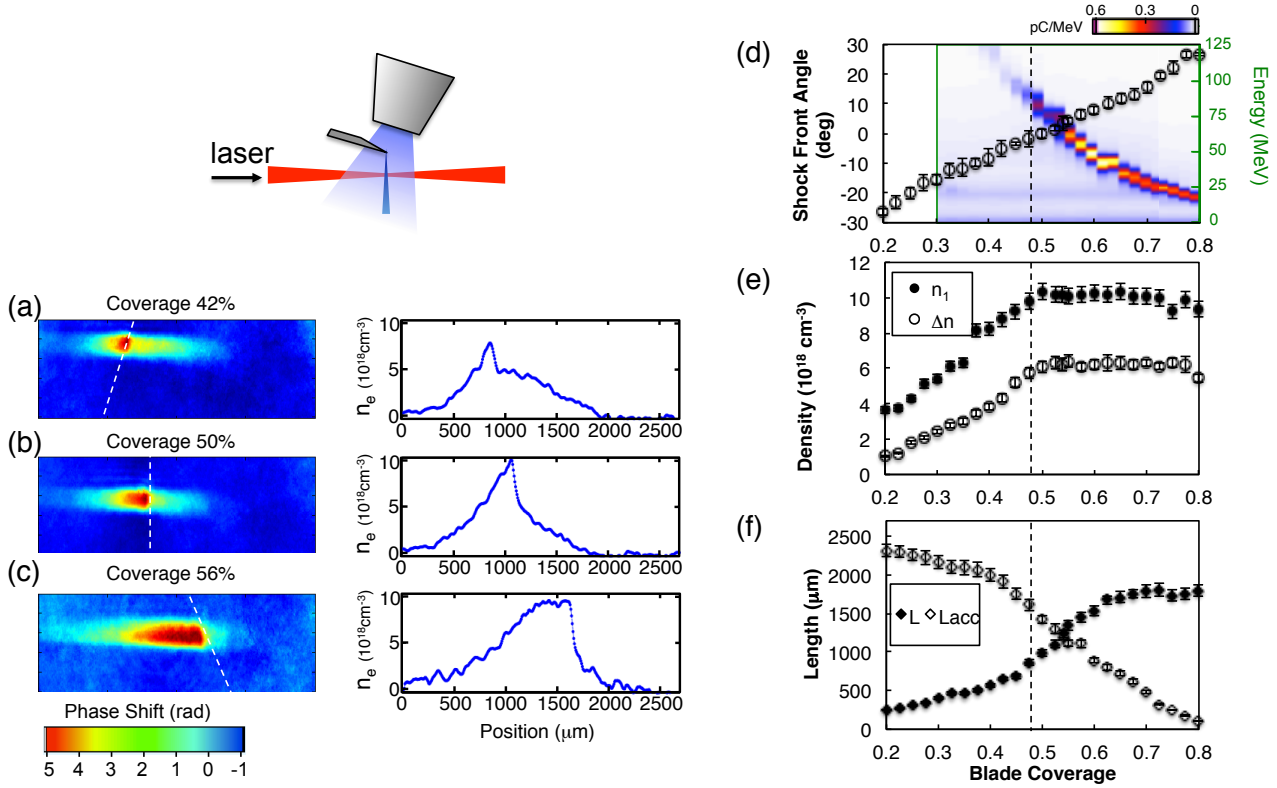

FIG. 3. The top picture shows a 30-degree pivoted jet-blade assembly in which the steepest shock is produced orthogonally to laser propagation. **(a)**, **(b)**, and **(c)**corresponds to a phase image and horizontal phase lineout at a particular blade coverage. The shock front (indicated with white dash line) can be seen near 0 degree. **(d)** Shock front angle and e-beam magnetic spectra, **(e)** shock density, n_1, and density drop, $\Delta n, (= n_1 - n_2)$ and **(f)** up-ramp width, L, and acceleration length, L_{acc}, versus blade coverage. Significant electron injection happens when blade coverage is more than 48%, which is around 0 degree shock angle.

with 1 J laser energy on target and average plasma density $n_e = 5 \times 10^{18}$ cm^{-3}, the central energy can be tuned continuously from 30 MeV to 120 MeV. In this blade scan, shock angle is varying from +10 to -10 degrees. The energy spread (FWHM) is even lower than 8% in this region near 50% blade coverage (where shock angle is straight, 0^o). At the straight shock point, by varying backing pressure from 100 psi to 300 psi (corresponding to n_e 3 to 7 $\times 10^{18}$ cm^{-3}) as shown in Fig. 6(b), the e-beam central energy can be tuned from 20 MeV to 200 MeV. E-beam tunability can be demonstrated in different energy regimes through blade scans at various levels of plasma density and laser energy. For example, by increasing the laser energy to 1.5 J on target and reducing the average plasma density down to 3 $\times 10^{18}$ cm^{-3} to match the self-guiding condition, e-beam central energy can be tuned continously via a blade scan to 300 MeV as shown in Fig. 6 (c). Under these conditions, the e-beam in Fig. 6 (c) displayed low energy spread, $\Delta E_{\rm FWHM}/E < 10\%$, 0.35 mrad poiting stability, and 1.5 mrad divergence.

Variations of e-beam energy width, $\Delta E_{\rm FWHM}$ across multiple parameters were analyzed to extract the dependence on up-ramp width, L, and peak density, n_1. $\Delta E_{\rm FWHM}$ was significantly reduced when the jet was translated vertically towards the laser (jet-to-laser distance decreased) as shown in Fig. 7 (a). The phase measurement simultaneously revealed a continuous change in shock structure, as shown in Fig. 7 (b). Up-ramp width decreased and n_1 increased as jet-to-laser distance decreased. On the other hand, we found in the pressure scan experiment, that $\Delta E_{\rm FWHM}$ can be reduced by decreasing backing pressure, as shown in Fig. 7 (c). However, under a pressure scan, the phase measurement revealed that both L and n_1 decreased as backing pressure decreased, as shown in Fig. 7 (d). The comparison between e-beam spectra and shock structures suggests that the variation of $\Delta E_{\rm FWHM}$ correlates to L and n_1, which were the two major varying parameters during the scan. The correlation between $\Delta E_{\rm FWHM}$ and L is shown in Fig. 7 (e). The data points from jet height scan (black) and pressure scan (red and green) match the same trend line (dashed line), indicating that L contributes to $\Delta E_{\rm FWHM}$. Given the different shock structures in a jet height scan (L increased as n_1 decreased) as compared to pressure scan (L and n_1 both increased as pressure was increased), we would expect the data points from the pressure scan to present a stronger trend than that from the jet height scan, if n_1 had contributed to

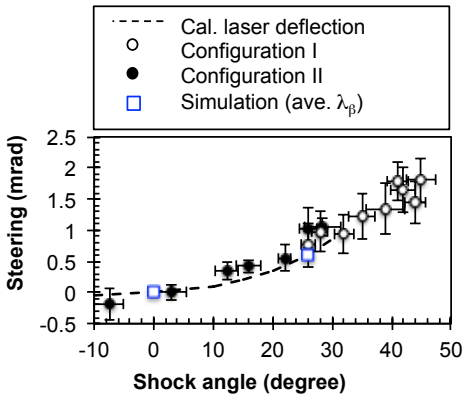

FIG. 4. Electron beam can be steered by shock front angle. Black (white) data points correspond to the experimental results using the straight shock (strongly tilted shock) configuration. Error bars denote standard error of mean shot-to-shot fluctuation. Blue square: average e-beam drift by integrating over betatron motion (λ_β) of 3D simulation results using 0 degree and 26 degree shock angle. Dashed line: calculated laser refraction.

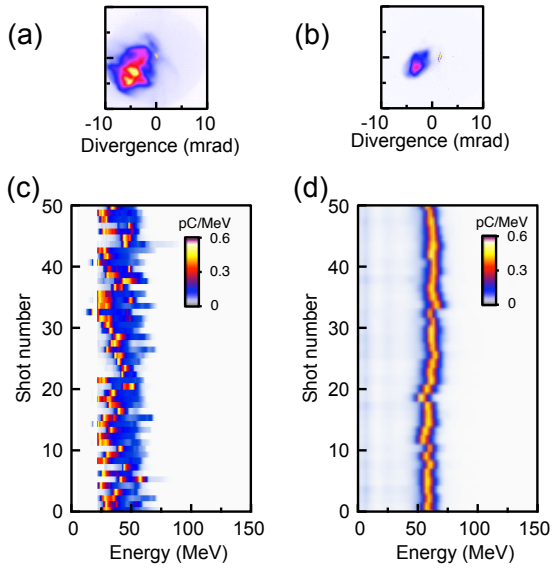

FIG. 5. Comparison of optimized acceleration results from tilt and straight shock: (a) spatial profile and (c) energy spectra of 50 consecutive shots from a 30 degree tilt shock. (b) spatial profile and (d) energy spectra of 50 consecutive shots from a straight shock.

$\Delta E_{\rm FWHM}$. Therefore, in this density regime ($P > P_{crit}$, $< 10^{19}$ cm^{-3}), $\Delta E_{\rm FWHM}$ can be controlled through adjusting up-ramp width in the shock structure. In addition, by adjusting both jet-to-laser distance and backing pressure, the length of L can be independently controlled while the density and length of L_{acc} remain constant. This allows decoupling of the effects of L and L_{acc}. Figure 7 (f) represents $\Delta E_{\rm FWHM}/E$ (black) and brightness (red), both of which vary as L increases, while the density and length of L_{acc} were stable at $\sim 3\times10^{18}$ cm^{-3} and ~ 1 mm. We found $\Delta E_{\rm FWHM}/E$ increased with L, however, e-beam brightness was maximized at $L = 1000$ μm (2 mm jet-to-laser distance and 170 psi backing pressure) given that the charge increased with L, and e-beam divergence was minimized at $L = 1000$ μm. Quasi-3D simulations using two density profiles ($L = 1000$ μm and 1500 μm) mimicking that from 1.7 mm and 2.9 mm jet-to-laser distance agree reasonably well with these experimental results [blue squares in Fig. 7 (e), black squares and red circles in Fig. 7 (f) represent simulation results]. We discuss the underlying physics of laser self-focusing over the up-ramp which drives this effect in Sec. V B below.

V. SIMULATIONS

To help understand the experimental results in Figs. 5 and 7, simulations were performed to demonstrate how different aspects of the shock profile impact laser propagation and the electron injection and acceleration processes. These simulations were used to verify shock profile effects on e-beam pointing, charge, energy, and energy spread as θ_s, L, and n_1 vary.

A. Shock angle vs. beam pointing

In order to study the influence of the shock angle, we performed 3D Cartesian electromagnetic PIC simulations using the WARP code.[60] The simulations were initialized with a fully Gaussian laser pulse $I_0\, e^{-2(x^2+y^2)/w_0^2}\, e^{-2\,t^2/\tau_0^2}$ of the same w_0 and τ_0 as for the experiment ($w_0 = 18$ μm, $\tau_{\rm FWHM} = \tau_0\sqrt{2\ln 2} = 45$ fs, and peak intensity of $I_0 = 5\times10^{18}$ W/cm^2), and were run in a $100\times100\times50$ μm domain ($200\times200\times2500$ cells). For simplification, we assumed a pre-ionized plasma. The plasma density had the form:

$$n_e(z) = \begin{cases} n_1 \exp\{-[(z-z_0)/L]^2]\}, & \text{for } z \le z_0 \\ n_1 \exp\{-[(z-z_0)/L_d]^2\}, & \text{for } z_0 \le z \le z_1 \\ n_2 \exp\{-[(z-z_1)/L_{acc}]^2\}, & \text{for } z > z_1 \end{cases}$$

Here, $n_1 = 10^{19}$ cm^{-3}, $n_2 = 4\times10^{18}$ cm^{-3}, $z_0 = 1450$ μm, $z_1 = 1500$ μm, $L = 800$ μm, $L_d = 44$ μm, and $L_{acc} = 600$ μm. This profile mimicked the shock measured at 48% blade coverage by the first configuration, resulting in a 26 degrees tilted shock, a 1450 μm up-ramp, rising from 10^{18} cm^{-3} to a peak of 10^{19} cm^{-3} density, followed by a 50 μm down-ramp transition to a density of 4×10^{18} cm^{-3}. In the case of a straight shock, the density transition (or shock front) was set parallel to the y-axis, whereas in the case of a tilted shock, the density transition was offset by 26 degrees from the y-axis. These density profiles are represented in Fig. 8(a).

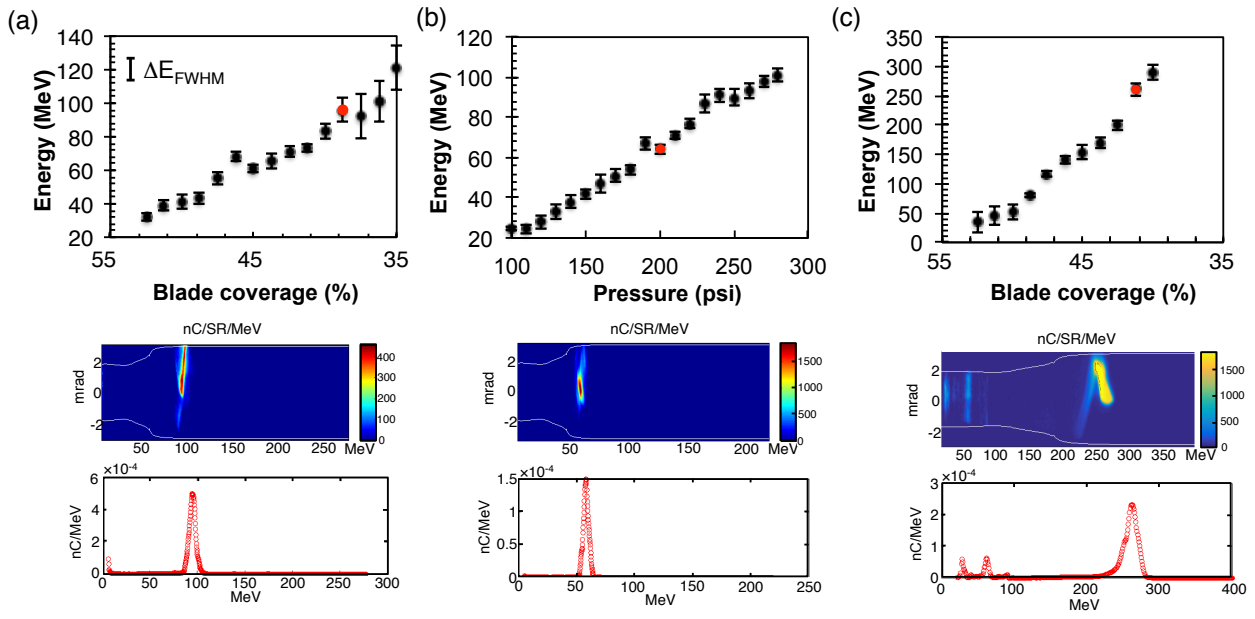

FIG. 6. In the straight shock configuration, e-beam central energy can be tuned with narrow energy spread maintained in three regimes: **(a)** blade scan at fixed plasma density, $n_e = 5 \times 10^{18}$ cm^{-3}, **(b)** density scan at fixed blade coverage (50%), and **(c)** blade scan at fixed plasma density, $n_e = 3 \times 10^{18}$ cm^{-3}. Top row: central energy as a function of blade coverage or pressure, middle row: E-beam magnetic spectrum images, bottom row: E-beam integrated spectrum lineout. The central energies shown in middle and bottom rows are indicated by red dots in top row. The error bars represent ΔE_{FWHM}.

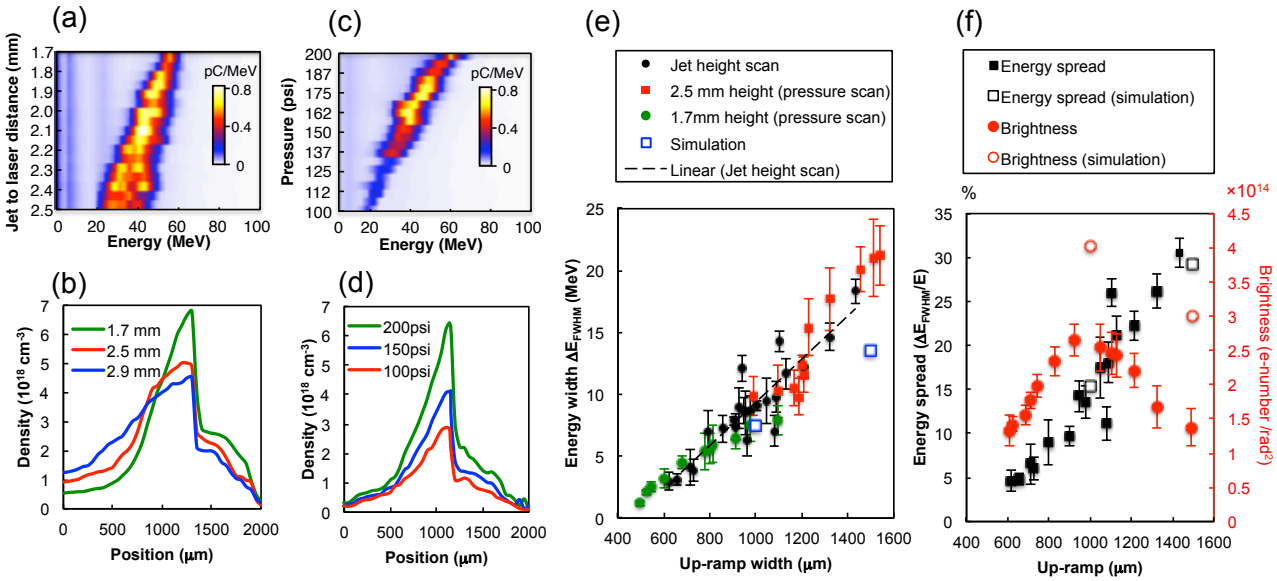

FIG. 7. **(a)** E-beam magnetic spectrum waterfall plot showing stacked lineout as the jet was translated vertically towards laser (jet-to-laser distance). Each horizontal line corresponds to an e-beam spectrum produced at a particular jet-to-laser distance. **(b)** Three shock density profiles taken at 1.7 mm (green), 2.1 mm (blue), and 2.9 mm (red) jet-to-laser distance. **(c)** E-beam magnetic waterfall plot as backing pressure was increased. **(d)** Three shock density profiles taken at 200 psi (green), 150 psi (blue), and 100 psi (red) backing pressure. **(e)** E-beam energy width (ΔE_{FWHM}) as a function of density up-ramp width. Data points represent the results from jet-to-laser distance scan (black) and pressure scan at 1.7 mm (green) and 2.5 mm (red) jet-to-laser distance. Blue squares represent simulation results. **(f)** E-beam energy spread, $\Delta E_{\mathrm{FWHM}}/E$ (black), and brightness, electron number/rad^2 (red), as a function of density up-ramp width. Empty squares and circles represent simulation results.

In the simulations, the laser polarization was set along the x axis, instead of the y axis because finite-difference

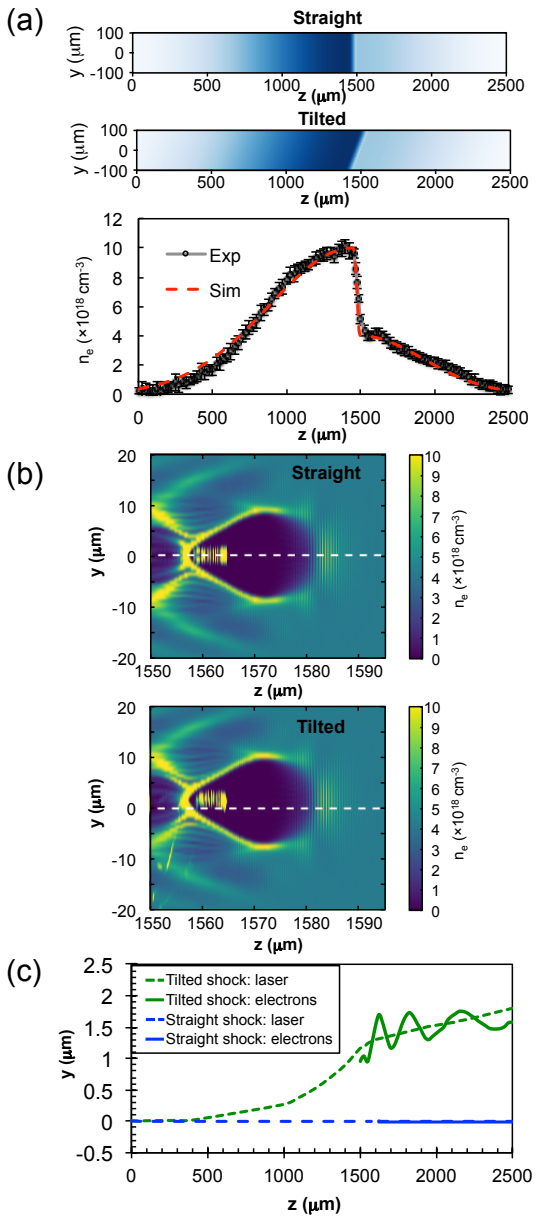

FIG. 8. 3D PIC simulations of e-beam steering by shock angle. **(a)** Two density profiles: straight shock and 26-degree tilted shock with same on-axis density lineout(red dashed line) vs. measurement (black dots). **(b)** Two snap shots representing the wakefield structure after 150μm propagation over the shock fronts. **(c)** Laser (dashed lines) and electron (solid lines) trajectories passing over the tilted shock (green) and the straight shock (blue).

PIC codes do not accurately reproduce the dynamics of relativistic electrons along the polarization axis, due to numerical artifacts.[61,62] Hence, by setting the polarization along x, instead of y, we ensured that these numerical artifacts did not affect the divergence and steering angle along the y axis, which are the quantities that we study here. By varying the longitudinal and transverse resolution, we verified that the transverse beam dynamics just after injection is numerically converged in the y direction (almost converged in the x, due to the above-mentioned numerical artifact).

Figure 8(b) shows two snapshots of different wakefield structures after the laser propagated 150 μm past the shock front. Because of the asymmetry of the tilted shock configuration, the electrons are injected off-axis rather than centered in that case. This implies that the electrons will have a higher betatron amplitude in the tilted shock configuration, as seen also in Fig. 8(c) (solid lines). This higher betatron amplitude could explain the greater fluctuations in pointing and divergence that were experimentally observed in this case.

Moreover, as the laser propagated through the 26-degree shock front in the simulations, it deviated away from the z-axis due to refraction in the asymmetric density distribution, as shown in Fig. 8(c) (dashed lines). This figure also shows that, in addition to their betatron motion, the electrons have an average drift, as they follow the laser trajectory. By integrating over betatron motion, 0 and 0.6 mrad average electron drift are inferred for the straight and 26-degree tilted shock respectively. These values agree well with measured results as shown in Fig. 4. In addition, the beam pointing in the y direction oscillates about the value 0.6 mrad, with an amplitude of oscillation of approximately $\pm$ 2.5 mrad, near the plasma exit at $z \sim 2.5$ mm. These oscillations could explain the observed fluctuations in beam pointing in the experiment, since shot-to-shot variations in e.g. gas density or laser intensity could result in fluctuations of the final betatron phase. From the amplitude of $\pm$ 2.5 mrad in the simulation, and under the coarse assumption that shot-to-shot fluctuations sample the final betatron phase uniformly between 0 and 2π, the expected peak fluctuation would be $\pm$ 2.5 mrad and the expected RMS fluctuations would be 1.8 mrad. By comparison, in the experiment, the peak fluctuations were $\pm$ 1.5 mrad, and the RMS fluctuations were 0.7 mrad. These values suggest the betatron oscilation observed in the experiment might fluctuate over a fraction of betatron period. For example, 1/4 λ_β, would make the statistics consitent with simulation results. Our further analysis suggest laser pointing and density fluctuation have much less contribution to the e-beam pointing fluctuation and a closer agreement and explanation would require a follow-up understanding of laser asymmetry, namely, pulse front tilt[63], and its impact on betatron phase.

B. Up-ramp width vs. energy spread

We further investigated the influence of up-ramp width, L, in the straight-shock configuration. This configuration is essentially cylindrically-symmetric, and thus we used the quasi-3D FBPIC code.[61] The parameters of the laser pulse (intensity profile and polarization) were identical to those of the previous section. The simulation

box in the (z, r) plane was 75×100 μm, with 3750×400 cells.

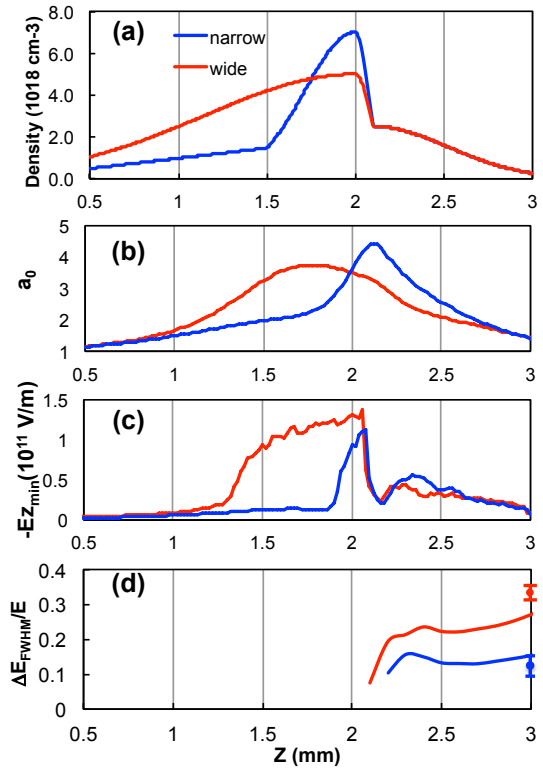

FIG. 9. Quasi-3D simulations of the up-ramp length. **(a)** Density profiles: a wide up-ramp (L = 1500 μm, $n_1 = 7\times10^{18}$ cm^{-3}, indicated as a red curve) and a narrow up-ramp (L = 1000 μm, $n_1 = 5 \times 10^{18}$ cm^{-3}, indicated as a blue curve) with identical acceleration length (L_{acc} = 800 μm, $n_2 = 3\times10^{18}$ cm^{-3}) were used for simulation. **(b)** The normalized vector potential a_0 of the drive pulse, **(c)** the peak longitudinal acceleration field, $-E_{z,min}$, and **(d)** electron energy spread, $\Delta E_{\rm FWHM}/E$, vary as a function of propagation distance. Blue and red data points represent the experimental measurements.

In the simulation setup, we mimicked two density profiles that were experimentally obtained at 1.7 mm and 2.9 mm jet-to-laser distance, as shown in Fig. 7(c). The profiles are presented in Fig. 9(a), showing a wide and low shock (red) with a 1500-μm L and a narrow and high shock (blue) with a 1000-μm L, while the down-ramp and L_{acc} regions were identical to each other in order to isolate up-ramp effect on the e-beam.

The simulations demonstrate that, in both the wide and narrow L profiles, w_0 decreases and a_0 increases as the laser pulse propagates through the up-ramp region, indicating that it undergoes self-focusing. Consequently, the peak accelerating field at the back of the bubble $E_{z,min}$ increases, as shown in Figs. 9(b) and (c). In the wide L profile, the laser self-steepening is enhanced, and as a consequence, drives higher wake amplitude, so the increase in $E_{z,min}$ is more pronounced as shown in Fig. 9 (c).

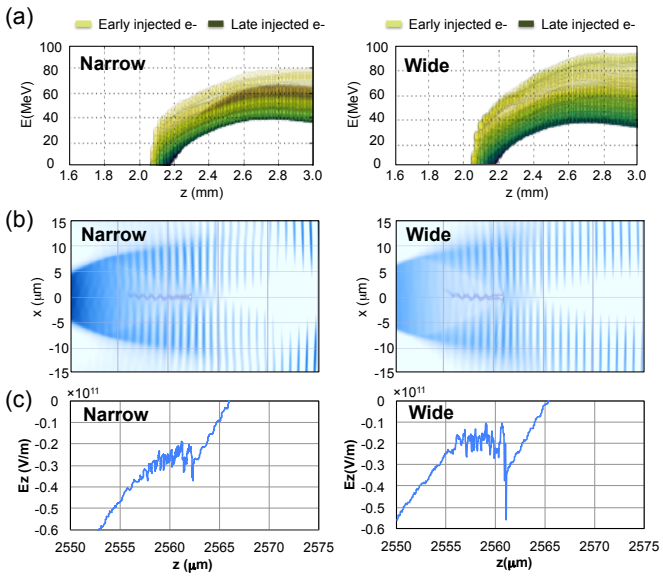

FIG. 10. Quasi-3D simulations of the wide and narrow up-ramp length. **(a)** Tracking of accelerated particle energy as a function of propagation distance. Light (dark) green depicts to early (late) injection time. **(b)** Snapshots of wake-field structure and injected electrons in the x - z plane, and **(c)** on-axis E_z field at the time the drive pulses passed the location at z = 2.6 mm.

As the electrons are injected in the down-ramp region, their energy spread is determined by the difference in acceleration between the electrons that are injected at the beginning of the down-ramp (which exit the accelerator with high energy), and those that are injected at the end of the down-ramp (which exit the accelerator with slightly lower energy). The electrons are injected earlier in the case of wide L, resulting in a longer bunch, which produces higher energy spread and approximately the same mean energy throughout L_{acc} ($z = 2 - 2.5$ mm). The energy spread in the simulations, defined as $\Delta E_{\rm FWHM}/E$, reproduces the experimentally measured energy spread with similar density profiles, as shown by the data points in Fig. 9(d).

Furthermore, due to the differing beam loading effects resulting from the wide and narrow L profiles, their respective bunches rotate in phase space differently as they accelerate. In the narrow L case, the trailing particles, indicated as dark green in Fig. 10 (a), cross over the early injected particles, indicated as yellow, at the position of z = 2.2 mm. This also explains why the energy spread is more compact in the narrow L case. Meanwhile, the absence of bunch rotation in the wide L case indicates that the beam loading effect is more pronounced during acceleration. This is confirmed by examining the E_z field inside the the bubble structure. Fig. 10 (b) and (c) show the 2-D and 1-D E_z field structure when the bubbles are propagating through the acceleration region from z = 2.5 mm to 2.6 mm. Over the region of the electron bunch,

the E_z field is almost leveled in the wide L case. These results suggest that energy spread can be controlled by adjusting the shock up-ramp width in this regime. However, in a separate and improbable scenario, additional simulations not shown here suggest that, were the peak density to increase significantly ($n_1 > 10^{19}$ cm^{-3} and $L < 500$ μm), energy spread would increase as a result. this regime does not correspond to the current experiment.

The overall injected charge is 20% higher in the wide L case. However, further analysis of simulation results shows that the charge brightness, defined as electron number over divergence angle ($\theta_x\theta_y$), is 25% higher in the narrow L case as shown by the red circles in Fig. 7 (f). The fact that narrower L produces lower charge but higher brightness also agrees with experimental observations shown by the red data dots in Fig. 7 (f).

VI. CONCLUSION

Our results demonstrate a highly controllable, tunable quasi-monoenergetic LPA based on shock-induced density down-ramp injection. We fully characterized the parameters of the shock structure in correlation with LPA performance and found that the shock angle steers e-beam pointing due to laser refraction and that wider up-ramp legnth correlates to higher e-beam energy spread resulting from earlier injection in the down-ramp region and more pronounced beam loading effect along the accleration field. Through experimentation, we were able to straighten the shock angle and reduce the up-ramp width, yielding a precisely-controlled e-beam with central energy tunability from 25 MeV to 300 MeV, 8% energy spread ($\Delta E_{\mathrm{FWHM}}/E$), 0.35 mrad rms pointing stability, and 1.5 mrad divergence. This LPA will be applied in ongoing MeV Thomson source[20] and FEL[27] experiments, leading the way to compact, affordable, highly directional narrow bandwidth x-ray or γ-ray sources with beneficial application to photo-nuclear spectroscopy,[64,65] radiation therapy,[66] and nuclear nonproliferation/homeland security,[67–69] among other areas.

VII. ACKNOWLEDGEMENT

This work was supported by the U.S. Department of Energy (DOE) Office of Science, Office of High Energy Physics under Contract No. DE-AC02-05CH11231; by the National Science Foundation under Grants No. PHY-1415596 and No. PHY-1632796; and by the U.S. DOE National Nuclear Security Administration, Defense Nuclear Nonproliferation R&D (NA22).

REFERENCES

[1] T. Tajima and J. M. Dawson, Phys. Rev. Lett. **43**(4), 267 (1979).

[2] E. Esarey, C. B. Schroeder, and W. P. Leemans, Rev. Mod. Phys. **81**, 1229 (2009).

[3] S. P. D. Mangles, C. D. Murphy, Z. Najmudin, A. G. R. Thomas, J. L. Collier, A. E. Dangor, E. J. Divall, P. S. Foster, J. G. Gallacher, C. J. Hooker, *et al.*, Nature **431**(7008), 535 (2004).

[4] C. G. R. Geddes, C. Toth, J. van Tilborg, E. Esarey, C. B. Schroeder, D. Bruhwiler, C. Nieter, J. Cary, and W. P. Leemans, Nature **431**(7008), 538 (2004).

[5] J. Faure, Y. Glinec, A. Pukhov, S. Kiselev, S. Gordienko, E. Lefebvre, J.-P. Rousseau, F. Burgy, and V. Malka, Nature **431**(7008), 541 (2004).

[6] N. A. M. Hafz, T. M. Jeong, I. W. Choi, S. K. Lee, K. H. Pae, V. V. Kulagin, J. H. Sung, T. J. Yu, K.-H. Hong, T. Hosokai, *et al.*, Nature Photonics **2**, 571 (2008).

[7] S. Kneip, S. R. Nagel, S. F. Martins, S. P. D. Mangles, C. Bellei, O. Chekhlov, R. J. Clarke, N. Delerue, E. J. Divall, G. Doucas, *et al.*, Phys. Rev. Lett. **103**, 035002 (2009), URL `https://link.aps.org/doi/10.1103/PhysRevLett.103.035002`.

[8] D. H. Froula, C. E. Clayton, T. Döppner, K. A. Marsh, C. P. J. Barty, L. Divol, R. A. Fonseca, S. H. Glenzer, C. Joshi, W. Lu, *et al.*, Phys. Rev. Lett. **103**, 215006 (2009), URL `https://link.aps.org/doi/10.1103/PhysRevLett.103.215006`.

[9] W. P. Leemans, B. Nagler, A. J. Gonsalves, C. Tóth, K. Nakamura, C. G. R. Geddes, E. Esarey, C. B. Schroeder, and S. M. Hooker, Nature Phys. **2**, 696 (2006).

[10] X. Wang, R. Zgadzaj, N. Fazel, Z. Li, S. A. Yi, X. Zhang, W. Henderson, Y.-Y. Chang, R. Korzekwa, H.-E. T. C.-H. Pai, *et al.*, Nat. Comm. **4**, 1988 (2013).

[11] H. T. Kim, K. H. Pae, H. J. Cha, J. Kim, T. J. Yu, J. H. Sung, S. K. Lee, T. M. Jeong, and J. Lee, Phys. Rev. Lett. **111**, 165002 (2013).

[12] W. P. Leemans, A. Gonsalves, H.-S. Mao, K. Nakamura, C. Benedetti, C. Schroeder, Cs. Tóth, J. Daniels, D. Mittelberger, S. Bulanov, *et al.*, Phys. Rev. Lett. **113**, 245002 (2014).

[13] H. T. Kim, V. Pathak, K. H. Pae, A. Lifschitz, F. Sylla, J. H. Shin, C. Hojbota, S. K. Lee, J. H. Sung, H. W. Lee, *et al.*, Scientific Reports **7**(1), 10203 (2017).

[14] A. Pukhov and J. Meyer-ter-Vehn, Appl. Phys. B **74**, 355 (2002).

[15] H. Schwoerer, B. Liesfeld, H.-P. Schlenvoigt, K.-U. Amthor, and R. Sauerbrey, Physical review letters **96**(1), 014802 (2006).

[16] K. T. Phuoc, S. Corde, C. Thaury, V. Malka, A. Tafzi, J. P. Goddet, R. C. Shah, S. Sebban, and A. Rousse, Nat. Phot. **6**, 308 (2012).

[17] S. Chen, N. D. Powers, I. Ghebregziabher, C. M. Maharjan, C. Liu, G. Golovin, S. Banerjee, J. Zhang, N. Cunningham, A. Moorti, *et al.*, Phys. Rev. Lett. **110**, 155003 (2013).

[18] N. D. Powers, I. Ghebregziabher, G. Golovin, C. Liu, S. Chen, S. Banerjee, J. Zhang, and D. P. Umstadter, Nat. Phot. **8**, 28 (2013).

[19] G. Sarri, D. Corvan, W. Schumaker, J. Cole, A. Di Piazza, H. Ahmed, C. Harvey, C. H. Keitel, K. Krushelnick, S. Mangles, *et al.*, Physical review letters **113**(22), 224801 (2014).

[20] C. G. Geddes, S. Rykovanov, N. H. Matlis, S. Steinke, J.-L. Vay, E. H. Esarey, B. Ludewigt, K. Nakamura, B. J. Quiter, C. B. Schroeder, *et al.*, Nuclear Instruments and Methods in Physics Research Section B: Beam Interactions with Materials and Atoms **350**, 116 (2015).

[21] H.-E. Tsai, X. Wang, J. M. Shaw, Z. Li, A. V. Arefiev, X. Zhang, R. Zgadzaj, W. Henderson, V. Khudik, G. Shvets, *et al.*, Physics of Plasmas **22**(2), 023106 (2015).

[22] K. Khrennikov, J. Wenz, A. Buck, J. Xu, M. Heigoldt, L. Veisz, and S. Karsch, Physical review letters **114**(19), 195003 (2015).

[23] C. Yu, R. Qi, W. Wang, J. Liu, W. Li, C. Wang, Z. Zhang, J. Liu, Z. Qin, M. Fang, *et al.*, Scientific reports **6** (2016).

[24] G. Golovin, S. Banerjee, C. Liu, S. Chen, J. Zhang, B. Zhao, P. Zhang, M. Veale, M. Wilson, P. Seller, *et al.*, Scientific reports **6**, 24622 (2016).

[25] M. Fuchs, R. Weingartner, A. Popp, Z. Major, S. Becker, J. Osterhoff, I. Cortrie, B. Zeitler, R. Hörlein, G. D. Tsakiris, *et al.*, Nature physics **5**(11), 826 (2009).

[26] Z. Huang, Y. Ding, and C. B. Schroeder, Phys. Rev. Lett. **109**, 204801 (2012).

[27] J. van Tilborg, S. Barber, F. Isono, C. Schroeder, E. Esarey, and W. Leemans, in *AIP Conference Proceedings* (AIP Publishing, 2017), vol. 1812, p. 020002.

[28] S. Steinke, J. van Tilborg, C. Benedetti, C. G. R. Geddes, C. B. Schroeder, J. Daniels, K. K. Swanson, A. J. Gonsalves, K. Nakamura, B. H. Shaw, *et al.*, Nature **530**, 190 (2016).

[29] M. Chen, Z.-M. Sheng, Y.-Y. Ma, and J. Zhang, J. Appl. Phys. **99**(5), 056109 (2006).

[30] A. Pak, K. A. Marsh, S. F. Martins, W. Lu, W. B. Mori, and C. Joshi, Phys. Rev. Lett. **104**(2), 025003 (2010).

[31] C. McGuffey, A. G. R. Thomas, W. Schumaker, T. Matsuoka, V. Chvykov, F. J. Dollar, G. Kalintchenko, V. Yanovsky, A. Maksimchuk, K. Krushelnick, *et al.*, Phys. Rev. Lett. **104**(2), 025004 (2010).

[32] C. E. Clayton, J. E. Ralph, F. Albert, R. A. Fonseca, S. H. Glenzer, C. Joshi, W. Lu, K. A. Marsh, S. F. Martins, W. B. Mori, *et al.*, Phys. Rev. Lett. **105**, 105003 (2010).

[33] C. Schroeder, J.-L. Vay, E. Esarey, S. Bulanov, C. Benedetti, L.-L. Yu, M. Chen, C. Geddes, and W. Leemans, Physical Review Special Topics-Accelerators and Beams **17**(10), 101301 (2014).

[34] S. K. Barber, J. van Tilborg, C. B. Schroeder, R. Lehe, H.-E. Tsai, K. K. Swanson, S. Steinke, K. Nakamura, C. G. R. Geddes, C. Benedetti, *et al.*, Phys. Rev. Lett. **119**, 104801 (2017).

[35] C. Kamperidis, V. Dimitriou, S. Mangles, A. Dangor, and Z. Najmudin, Plasma Physics and Controlled Fusion **56**(8), 084007 (2014).

[36] M. Chen, E. Esarey, C. Schroeder, C. Geddes, and W. Leemans, Physics of Plasmas **19**(3), 033101 (2012).

[37] J. Liu, C. Xia, W. Wang, H. Lu, C. Wang, A. Deng, W. Li, H. Zhang, X. Liang, Y. Leng, *et al.*, Physical review letters **107**(3), 035001 (2011).

[38] B. Pollock, C. Clayton, J. Ralph, F. Albert, A. Davidson, L. Divol, C. Filip, S. Glenzer, K. Herpoldt, W. Lu, *et al.*, Physical review letters **107**(4), 045001 (2011).

[39] G. Golovin, S. Chen, N. Powers, C. Liu, S. Banerjee, J. Zhang, M. Zeng, Z. Sheng, and D. Umstadter, Physical Review Special Topics-Accelerators and Beams **18**(1), 011301 (2015).

[40] J. Faure, C. Rechatin, A. Norlin, A. Lifschitz, Y. Glinec, and V. Malka, Nature **444**(7120), 737 (2006).

[41] E. Esarey, R. F. Hubbard, W. P. Leemans, A. Ting, and P. Sprangle, Phys. Rev. Lett. **79**(14), 2682 (1997).

[42] G. Fubiani, E. Esarey, C. B. Schroeder, and W. P. Leemans, Phys. Rev. E **70**(1), 016402 (2004).

[43] S. Bulanov, N. Naumova, F. Pegoraro, and J. Sakai, Phys. Rev. E **58**(5), R5257 (1998).

[44] C. G. R. Geddes, K. Nakamura, G. R. Plateau, Cs. Tóth, E. Cormier-Michel, E. Esarey, C. B. Schroeder, J. R. Cary, and W. P. Leemans, Phys. Rev. Lett. **100**(21), 215004 (2008).

[45] J. Faure, C. Rechatin, O. Lundh, L. Ammoura, and V. Malka, Phys. Plasmas **17**(8), 083107 (2010).

[46] K. Schmid, A. Buck, C. M. S. Sears, J. M. Mikhailova, R. Tautz, D. Herrmann, M. Geissler, F. Krausz, and L. Veisz, Phys. Rev. ST Accel. Beams **13**(9), 091301 (2010).

[47] A. J. Gonsalves, K. Nakamura, C. Lin, D. Panasenko, S. Shiraishi, T. Sokollik, C. Benedetti, C. B. Schroeder, C. G. R. Geddes, J. van Tilborg, *et al.*, Nature Phys. **7**, 862 (2011).

[48] A. Buck, J. Wenz, J. Xu, K. Khrennikov, K. Schmid, M. Heigoldt, J. M. Mikhailova, M. Geissler, B. Shen, F. Krausz, *et al.*, Phys. Rev. Lett. **110**, 185006 (2013).

[49] E. Guillaume, A. Döpp, C. Thaury, K. T. Phuoc, A. Lifschitz, G. Grittani, J.-P. Goddet, A. Tafzi, S.-W. Chou, L. Veisz, *et al.*, Physical review letters **115**(15), 155002 (2015).

[50] C. Thaury, E. Guillaume, A. Lifschitz, K. T. Phuoc, M. Hansson, G. Grittani, J. Gautier, J.-P. Goddet, A. Tafzi, O. Lundh, *et al.*, Scientific reports **5** (2015).

[51] K. Swanson, H.-E. Tsai, S. Barber, R. Lehe, H.-S. Mao, S. Steinke, J. van Tilborg, K. Nakamura, C. Geddes, C. Schroeder, *et al.*, Phys. Rev. Accel. Beams **20**, 051301 (2017).

[52] C. Benedetti, C. Schroeder, E. Esarey, F. Rossi, and W. Leemans, Physics of Plasmas **20**(10), 103108 (2013).

[53] E. Esarey and M. Pilloff, Phys. Plasmas **2**(5), 1432 (1995).

[54] H.-S. Mao, K. Swanson, H.-E. Tsai, S. Barber, S. Steinke, J. van Tilborg, C. Geddes, and W. Leemans, in *AIP Conference Proceedings* (AIP Publishing, 2017), vol. 1812, p. 040007.

[55] T. C. Adamson and J. Nicholls, J. Aerosp. Sci **26**(1), 16 (1959).

[56] G. Plateau, N. Matlis, C. Geddes, A. Gonsalves, S. Shiraishi, C. Lin, R. van Mourik, and W. Leemans, Review of Scientific Instruments **81**(3), 033108 (2010).

[57] A. Buck, K. Zeil, A. Popp, K. Schmid, A. Jochmann, S. Kraft, B. Hidding, T. Kudyakov, C. Sears, L. Veisz, *et al.*, Review of Scientific Instruments **81**(3), 033301 (2010).

[58] K. Nakamura, W. Wan, N. Ybarrolaza, D. Syversrud, J. Wallig, and W. P. Leemans, Rev. Sci. Instrum. **79**, 053301 (2008).

[59] K. Nakamura, A. J. Gonsalves, C. Lin, A. Smith, D. Rodgers, R. Donahue, W. Byrne, and W. P. Leemans, Phys. Rev. ST Accel. Beams **14**, 062801 (2011).

[60] J.-L. Vay, D. Grote, R. Cohen, and A. Friedman, Computational Science & Discovery **5**(1), 014019 (2012).

[61] R. Lehe, M. Kirchen, I. A. Andriyash, B. B. Godfrey, and J.-L. Vay, Computer Physics Communications **203**, 66 (2016).

[62] R. Lehe, C. Thaury, E. Guillaume, A. Lifschitz, and V. Malka, Phys. Rev. ST Accel. Beams **17**, 121301 (2014).

[63] D. Mittelberger, M. Thévenet, K. Nakamura, R. Lehe, A. Gonsalves, C. Benedetti, and W. Leemans, in *APS Meeting Abstracts* (2017).

[64] E. C. Schreiber, R. Canon, B. Crowley, C. Howell, J. Kelley, V. Litvinenko, S. Nelson, S. Park, I. Pinayev, R. Prior, *et al.*, Physical Review C **61**(6), 061604 (2000).

[65] E. Kwan, G. Rusev, A. Adekola, F. Dönau, S. Hammond, C. Howell, H. Karwowski, J. Kelley, R. S. Pedroni, R. Raut, *et al.*, Physical Review C **83**(4), 041601 (2011).

[66] K. Weeks, V. Litvinenko, and J. Madey, Medical physics **24**(3), 417 (1997).

[67] T. Jannson, M. Gertsenshteyn, V. Grubsky, P. Amouzou, and R. Koziol, in *Sensors, and Command, Control, Communications, and Intelligence (C3I) Technologies for Homeland Security and Homeland Defense VI* (International Society for Optics and Photonics, 2007), vol. 6538, p. 65380A.

[68] S. Chen, G. Golovin, C. Miller, D. Haden, S. Banerjee, P. Zhang, C. Liu, J. Zhang, B. Zhao, S. Clarke, *et al.*, Nuclear Instruments and Methods in Physics Research Section B: Beam Interactions with Materials and Atoms **366**, 217 (2016).

[69] C. Geddes, B. Ludewigt, J. Valentine, B. Quiter, M.-A. Descalle, G. Warren, M. Kinlaw, S. Thompson, D. Chichester, C. Miller, *et al.*, *Impact of Monoenergetic Photon Sources on Nonproliferation Applications Final Report*, Tech. Rep., Idaho National Laboratory (INL), Idaho Falls, ID (United States) (2017).